Monthly Notices of the ROYAL ASTRONOMICAL SOCIETY

MNRAS **547,** 1–14 (2026)
Advance Access publication 2026 February 26

https://doi.org/10.1093/mnras/stag401

BlackTHUNDER strikes twice: Balmer-line absorption in an overmassive Little Red Dot at $z = 7.04$

Francesco D'Eugenio [1,2★] Roberto Maiolino [1,2,3] Michele Perna [4] Hannah Übler [5] Xihan Ji [1,2] William McClymont [1,2] Sophie Koudmani [1,6] Debora Sijacki [1,7] Ignas Juodžbalis [1,2] Jan Scholtz,[1,2] Jake S. Bennett [8] Andrew J. Bunker [9] Stefano Carniani [10] Stéphane Charlot [11] Giovanni Cresci [12] Emma Curtis-Lake [6] Elena Dalla Bontà [13,14,15] Kohei Inayoshi [16] Gareth C. Jones [1,2] Jianwei Lyu [17] Alessandro Marconi [12,18] Giovanni Mazzolari [19,20] Erica J. Nelson,[21] Eleonora Parlanti [5,10] Brant E. Robertson [22] Raffaella Schneider [23] Charlotte Simmonds [1,2] Sandro Tacchella [1,2] Giacomo Venturi [10] Chris Willott [24] Joris Witstok [25,26] and Callum Witten [27]

Affiliations are listed at the end of the paper

Accepted 2026 February 20. Received 2026 February 9; in original form 2025 March 15

ABSTRACT

James Webb Space Telescope (*JWST*) has revealed a population of 'Little Red Dots' (LRDs): compact, red objects at redshifts $z = 2$-9 with 'v'-shaped spectral energy distributions, broad permitted lines, and, often, hydrogen Balmer absorption. We use NIRSpec/IFS data from the BlackTHUNDER survey to study the Hα line in the LRD Abell2744-QSO1 at $z = 7.04$, which is a confirmed active galactic nucleus (AGN) due to time-variable equivalent width (EW) in its broad emission lines. The Hα spectral profile is non-Gaussian, requiring at least two Gaussian components. We also detect a narrow-line Gaussian component, and strong Hα absorption (EW relative to the continuum $\sim 22^{-7}_{+12}$Å), confirming a connection between the strong Balmer break and line absorption. The absorber is at rest with respect to broad Hα , suggesting that the gas cannot be interpreted as an inflow or outflow, forming instead a long-lived structure. Its velocity dispersion is $\sigma_{\rm abs} = 110^{+20}_{-10}$ km s^{-1}, consistent with the value inferred from the analysis of the Balmer break. Based on Hα , we infer a black hole mass of $\log(M_\bullet/{\rm M}_\odot) = 7.2$, smaller but close to the previous estimates based on Hβ . The Eddington ratio is 0.09. Combining the high signal-to-noise ratio of the narrow Hα line with the spectral resolution $R = 3,700$ of the G395H grating, we infer a narrow-line intrinsic dispersion $\sigma_{\rm n} = 22^{+5}_{-6}$ km s^{-1} , which places a stringent constraint on the black hole-to-dynamical mass ratio of this system to be $M_\bullet/M_{\rm dyn} = 0.15$-1.2, confirming the overmassive nature of the black hole and potentially leaving little room for a host galaxy.

Key words: galaxies: active – galaxies: high-redshift – quasars: supermassive black holes.

1 INTRODUCTION

A key question in galaxy evolution is whether supermassive black holes (SMBHs) and their host galaxies grow in tandem or if one forms first (M. J. Rees 1984; M. A. Latif & A. Ferrara 2016; K. Inayoshi, E. Visbal & Z. Haiman 2020). Did massive SMBH seeds emerge early, perhaps via direct collapse of pristine gas clouds (e.g. V. Bromm & A. Loeb 2003; M. C. Begelman, M. Volonteri & M. J. Rees 2006), or did star clusters and proto-galaxies accumulate mass first, fuelling the growth of lower-mass seeds, for example via runaway collisions (e.g. S. F. Portegies Zwart et al. 1999)? This question is fundamental for our understanding of the link between SMBHs and galaxies. At redshifts $z = 0$-2, SMBH masses ($M_\bullet$) correlate tightly with galaxy properties such as stellar velocity dispersion ($M_\bullet$–σ relation; L. Ferrarese & D. Merritt 2000; K. Gebhardt et al. 2000) and stellar or bulge mass ($M_\bullet$–$M_\star$ relation; A. Marconi & L. K. Hunt 2003; J. Kormendy & L. C. Ho 2013; N. J. McConnell & C.-P. Ma 2013; A. E. Reines & M. Volonteri 2015, hereafter RV15; R. P. Saglia et al. 2016; E. Dalla Bontà et al. 2025, hereafter DB25; Y. Sun et al. 2025). These correlations suggest a co-evolutionary link, where accreting SMBHs regulate star formation through powerful feedback (S. Veilleux, G. Cecil & J. Bland-Hawthorn 2005; A. C. Fabian 2012; F. Fiore et al. 2017; S. Veilleux et al. 2020), while galaxies, in turn, shape SMBH growth by modulating the gas supply for accretion, for instance by facilitating angular momentum loss, by altering the metal content and thermodynamic properties of the gas, and not least via star formation and supernova feedback (Y. Dubois et al. 2015; J. Silk 2017; M. Trebitsch et al. 2018; S. Koudmani, D. Sijacki & M. C.

★ E-mail: francesco.deugenio@gmail.com

Smith 2022). While efficiently accreting SMBHs powering active galactic nuclei (AGNs) are readily observable at high redshifts, the properties of their host galaxies remain uncertain – especially in the low-mass regime most relevant to understanding the origins of galaxies and SMBHs.

The advent of *James Webb Space Telescope* (*JWST*) enables direct observations of low-mass galaxies ($M_\star > 10^6\,M_\odot$) and SMBHs ($M_\bullet > 10^6 M_\odot$) at $z > 5$, offering new insights into their co-evolution. Recent discoveries reveal a large population of accreting SMBHs in low-mass galaxies at these redshifts (J. Matthee et al. 2024), with many appearing overmassive relative to their hosts' stellar mass (e.g. Y. Harikane et al. 2023; D. D. Kocevski et al. 2023; V. Kokorev et al. 2023; H. Übler et al. 2023; R. Maiolino et al. 2024). While $M_\star$ measurements in AGN-dominated systems remain uncertain, observations of faint SMBHs with low accretion rates support this trend (A. C. Carnall et al. 2023; I. Juodžbalis et al. 2024b). Notably, SMBHs at $z > 5$ may still lie on the local $M_\bullet$–σ relation (R. Maiolino et al. 2024), suggesting a degree of co-evolution *before* the onset of the local $M_\bullet$–$M_\star$ relation, which may happen at later epochs and/or higher mass ranges (J. Li, Y. Shen & M.-Y. Zhuang 2025; Y. Sun et al. 2025), but could hold already for the total baryonic mass (W. McClymont et al. 2026).

In addition to a possible departure from local scaling relations, several broad-line AGNs display strong Balmer breaks; if these spectral features arise from evolved stellar populations (a few hundred Myr and older), they would imply the existence of massive, old galaxies 600 Myr after the big bang (B. Wang et al. 2024, 2025) with extremely high surface densities (J. F. W. Baggen et al. 2024; Y. Ma et al. 2025b). Alternatively, these Balmer breaks could arise from dense gas absorption (K. Inayoshi & R. Maiolino 2025) along the line of sight to the SMBH. The discovery of Abell2744-QSO1 (L. J. Furtak et al. 2023, 2024) enabled us to break this degeneracy. The continuum of this source cannot be well reproduced by stellar-population spectra alone (Y. Ma et al. 2025b, at least not without invoking ad hoc attenuation laws). Subsequent *JWST* observations have revealed that the equivalent widths (EWs) of the broad lines are time variable (L. J. Furtak et al. 2025; X. Ji et al. 2025, hereafter J25), ruling out a stellar origin (e.g. J. F. W. Baggen et al. 2024; M. Kokubo & Y. Harikane 2025). Furthermore, time variability of the rest-frame optical continuum (J25) implies an AGN origin (but see L. J. Furtak et al. 2025 for a different view). Even more importantly, the narrow Hβ and [O III] λ5007 emission lines impose an upper limit on $M_{\rm dyn}$ that is one order of magnitude lower than the $M_\star$ inferred when assuming a stellar origin of the Balmer break.

One of the key predictions of J25 is that a strong, smooth Balmer break (with Balmer-break index ≈ 2.3; K. Inayoshi & R. Maiolino 2025) – associated with micro-turbulence of order 100 km s^{-1} – would produce equally strong Balmer line absorption with comparable broadening and high EWs. Indeed, several Little Red Dots (LRDs) have been reported to display high-EW Balmer-line absorption (I. Juodžbalis et al. 2024a; I. Labbe et al. 2024; J. Matthee et al. 2024; A. J. Taylor et al. 2025; B. Wang et al. 2024, 2025). In contrast, in the stellar scenario, since micro-turbulence is relatively low ($\lesssim 15$ km s^{-1} in the relevant stellar spectral types; K. C. Smith & I. D. Howarth 1998), line broadening is dominated by Gaussian-like stellar kinematics, resulting in significantly narrower line widths and much lower EWs (although non-Gaussian tails are still observed, due to pressure broadening). While J25 tentatively report Hβ absorption, their measurement is only at the 3σ significance level, due to the low signal-to-noise ratio (SNR) of the underlying broad line. Confirming this absorption is crucial, because its presence is a key prediction of the gas-absorber hypothesis, and because, if present, it would enable probing the kinematics of the gas cloud.

In this work, we present a re-analysis of the BlackTHUNDER high-resolution NIRSpec observations from J25, focusing on the much brighter Hα line, which we recover using a custom reduction procedure that extends beyond the nominal wavelength range calibration of NIRSpec. After describing the new data reduction and analysis (Section 2), we report three key findings (Section 3): non-Gaussian broad-Hα emission, a strong rest-frame Hα absorber, and an even more stringent upper limit on $M_{\rm dyn}$. We conclude with a discussion of our results and their implications (Sections 4 and 5).

Throughout this work, we assume a flat Lambda cold dark matter (λCDM) cosmology from Planck Collaboration VI (2020) and a G. Chabrier (2003) initial mass function. All EWs are in the rest frame.

2 DATA AND ANALYSIS

High-resolution spectroscopy of Abell2744-QSO1 covers Hα at observed wavelength $\lambda = 5.278\,\mu$m (spectral resolution $R = 3700$). These data were obtained by the programme Black holes in THe early Universe aNd their DensE surRoundings (BlackTHUNDER; *JWST* proposal PID 5015; PIs H. Übler and R. Maiolino) using the NIRSpec spectrograph (P. Jakobsen et al. 2022) in integral field spectroscopy mode (IFS; T. Böker et al. 2022). Here, we use only the G395H grating observations, consisting of 14 dithered integrations using the medium-dither cycling to offset fail-open shutters from the interloping micro-shutter assembly (MSA; P. Ferruit et al. 2022; K. Bechtold et al. 2024). We used the improved reference sampling and subtraction (IRS^2) readout mode (B. J. Rauscher et al. 2012), to minimize amplifier noise ('pink' or $1/f$ noise; S. H. Moseley et al. 2010; B. J. Rauscher et al. 2017). Each integration consisted of 23 groups and one exposure, giving 1692 s per dithered exposure and a total on-source exposure time of $1692.3 \times 14 = 23,692$ s.

For the data reduction, we use the procedure described in M. Perna et al. (2023), but we start from the JWST pipeline version 1.17.1 and context file 1303. At $z = 7.04$, Hα falls at $\lambda = 5.278\,\mu$m, just outside the calibrated range of the NIRSpec G395H grating, which reaches $\lambda < 5.27\,\mu$m. Moreover, the high-velocity wings of broad-Hα emission can easily reach up to $\lambda = 5.32\,\mu$m. However, since the low-pass F290LP is not suppressing long wavelengths, and since the grating transmission does not drop sharply, Hα is readily observable on the detector. We therefore extract the data by extrapolating the flat-field curves and wavelength solution beyond the nominal range. Due to the small extrapolation (only 95 spectral pixels between $\lambda = 5.27\,\mu$m and $5.34\,\mu$m), and thanks to the well characterized behaviour of the grating, the error on the wavelength solution is expected to be negligible. Similarly, the line-spread function is obtained from the grating equation, so we expect no significant deviation from the pre-flight characterization of the instrument (P. Jakobsen et al. 2022).

2.1 Spectral extraction

We use the optimal extraction method to obtain the 1D spectrum (K. Horne 1986). In principle, we would measure the spatial

profile directly from the datacube, but in practice the resulting profile shapes are too noisy. Therefore, we use a 2D Gaussian tracing the point spread function (PSF) of the NIRSpec/IFS. The aperture has elliptical shape with fixed position angle 25° and axis ratio $q = 0.8$ (following the elongated PSF shape and slice orientation; F. D'Eugenio et al. 2024a). The semimajor axis is wavelength dependent, following new empirical measurements (F. D'Eugenio et al. 2026; G. C. Jones et al. 2026).

Within two spectral pixels on either side of narrow H β , [O III] $\lambda\lambda$4959, 5007, and H α , we use the spatial profile measured from the narrow H α line, which is more extended than the PSF (R. Maiolino et al. 2025a; I. Juodžbalis et al. 2026a).

If we replace our analysis with a large aperture of semimajor axis 0.25 arcsec (e.g. X. Ji et al. 2025) our results are unchanged, but the spectral SNR for the broad lines is lower than for the optimal extraction.

The spectrum is shown in Fig. 1, with the data in black and the best-fitting model in red. While the model is described in the next sections, here we observe that the continuum blueward and redward of H α is described well by a linear fit, similar to other LRDs and broad-line AGN (over an equally narrow spectral range; e.g. J. E. Greene et al. 2024; I. Juodžbalis et al. 2024a, 2024b; A. J. Taylor et al. 2025). This agreement lends confidence to the accuracy of our extrapolated flux calibration. Nevertheless, since our $M_\bullet$ measurements are sensitive primarily to the width of the broad H α , with only a sub-linear dependence on the line flux, our main results are not driven by possible flux-calibration errors.

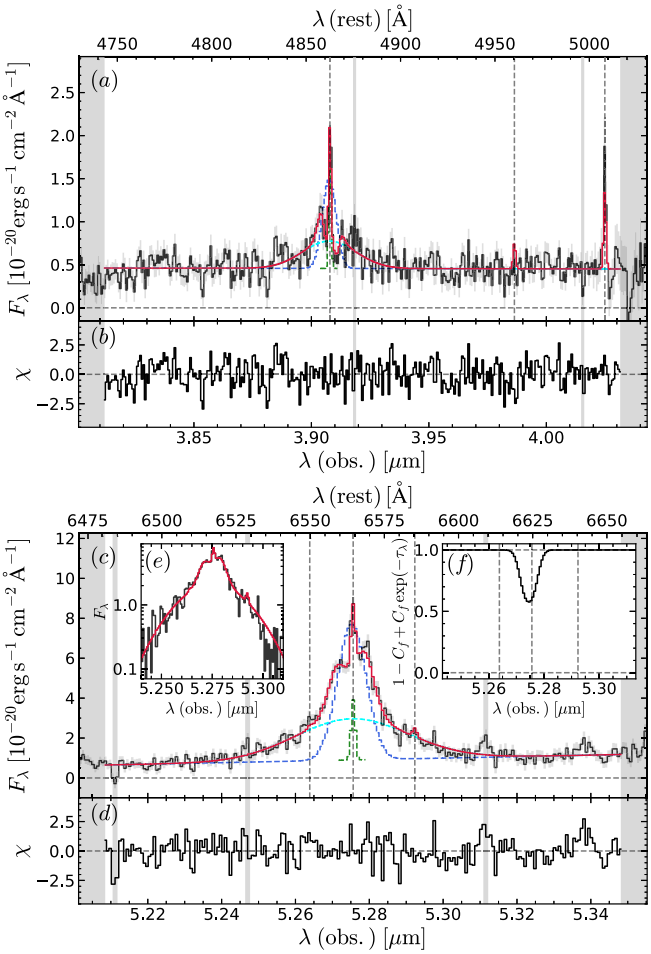

Figure 1. Detail of the BlackTHUNDER point-source aperture spectrum (black) around H β and [O III] $\lambda\lambda$4959, 5007 (panel a) and H α (panel c). The red line is the maximum-likelihood model (Section 2), with the χ residuals shown in panels (b) and (d). The maximum-likelihood model includes the continuum and two broad Gaussians (cyan and blue), subject to Balmer-line absorption, and an unabsorbed narrow Gaussian (green). The grey vertical bands are masked spectral regions, while the vertical dashed lines mark the rest-frame wavelengths of the modelled emission lines. For H α , we show the narrow-component Gaussian in green and the two unabsorbed broad Gaussians in cyan and blue. The wings of H α are highlighted in panel (e). There is clear evidence of line absorption in H α and of a narrow component with $\sigma_n = 22$ km s^{-1}. The absorption profile (including partial covering factor) is shown in panel (f).

2.2 Spectral modelling

In this section we describe the fiducial model, which employs two broad Gaussians to model the broad lines. For clarity, we anticipate that the model choice is not motivated by statistical preference, but by the recent results of R. Maiolino et al. (2025a) and I. Juodžbalis et al. (2026a), who establish that the intermediate-width broad component in Abell2744-QSO1 is spatially resolved, while the broadest broad component is not, motivating two distinct Gaussians. Alternative models are introduced in Section 3 or in the Appendix.

We model the narrow lines with Gaussians, using the same redshift and intrinsic velocity dispersion σ_n for all lines. We further constrain the [O III] and [N II] doublet ratios to 0.336 (P. J. Storey & C. J. Zeippen 2000) and 0.328, respectively (I. Dojčinović, J. Kovačević-Dojčinović & L. Č. Popović 2023), hence the narrow-line model requires six parameters: z_n, σ_n, and the fluxes of H β , [O III] λ5007, H α and [N II] λ6583. In principle, the narrow hydrogen, [O III] and [N II] lines could arise from different regions with different kinematics, but the limited SNR of our data (and the non-detection of [N II] $\lambda\lambda$6548, 6583) prevent us from testing this hypothesis. We model the continuum piecewise in each spectral window using a first-order polynomial each, requiring four more parameters in total. For the broad Balmer lines we use a double Gaussian, given the clearly non-Gaussian shape of H α (Fig. 1c). The two Gaussians representing broad H α share the same centroid, specified by a common free parameter representing the velocity offset v_b between the broad and narrow lines. We have two independent full width at half-maximum (FWHM) values, while the flux is parametrized by the total unabsorbed flux of H α and by the flux ratio between the narrowest Gaussian and the total unabsorbed line flux. There are thus five more free parameters.

One additional parameter is required to model the broad H β , which also consists of two Gaussians, but whose velocity, FWHM and flux ratio are constrained to be identical to those for H α . In other words, the broad H α and H β models share the same kinematics and internal flux ratio, and the only additional parameter for broad H β is the total unabsorbed H β flux.

In principle, the flux ratio of the two broad Gaussians could be different between H β and H α , for instance if these two Gaussians reflect different kinematic components, which could be subject to different excitation mechanisms and dust attenuation. However, the number of parameters for H β is effectively limited by the SNR of the data (J25). Finally, we add a dense hydrogen absorber, with a common covering factor C_f, the same velocity dispersion σ_{abs}, and different velocity offsets $v_{abs,\,H\beta}$ and $v_{abs,H\alpha}$ for H β and H α (the velocity offset is relative to the redshift of

the narrow lines). The residual intensity at wavelength λ is given by

$$I(\lambda)/I_0(\lambda) = 1 - C_f + C_f \times \exp\left(-\tau(k;\ \lambda)\right)$$
$$\tau(k;\ \lambda) = \tau_0(k) \times f[v(\lambda)], \quad (1)$$

where $I_0(\lambda)$ is the spectral flux density before absorption, $\tau_0(k)$ is the optical depth at the centre of the line (with $k =$ H β or H α), and $f[v(\lambda)]$ is the velocity distribution of the absorbing atoms, assumed to be a Gaussian probability distribution. $I_0(\lambda)$ consists of both the continuum (dominated by the accretion disc; J25) and the broad-line region (BLR). The different velocity of the H β and H α absorptions is motivated by visual inspection of the data, and is justified by the observation of dense absorbers with different effective velocities for H α and H β in higher-SNR observations of LRDs (F. D'Eugenio et al. 2025; X. Ji et al. 2026; X. Lin et al. 2026).

For each optimization step, the trial model is convolved with the wavelength-dependent line spread function and is then integrated pixel-by-pixel. For model inference we use a Bayesian approach, with flat, non-informative priors around all parameters. The posterior probabilities are sampled using the Markov chain Monte Carlo method (see F. D'Eugenio et al. 2026 for more details).

3 RESULTS

The maximum-likelihood model is shown in Fig. 1. The H α narrow line is clearly detected, with the observed flux $\mu F_{\rm n}$(H α) being 6σ away from 0 (Table 1). Together with weaker H β and [O III] λ5007, the observed wavelength of narrow H α implies a redshift $z = 7.0366 \pm 0.0001$. The intrinsic width of the narrow lines is extremely small, $\sigma_{\rm n} = 22^{+5}_{-6}$ km s^{-1}, corresponding to 0.6 times the spectral resolution ($FWHM = 81$ km s^{-1}, $\sigma_R = 34$ km s^{-1} at the observed wavelength of H α). While the inferred $\sigma_{\rm n}$ is small, a simple analytical calculation tells us that, given a Gaussian line spread function (LSF) with $R = 3700$ and a line detection with SNR of 6, we can detect a spectral broadening of $\sigma = 22$ km s^{-1} at 2σ (L. Zhou et al. 2017), comparable to the posterior probability on $\sigma_{\rm n}$ (i.e. 22/6 = 3σ significance). The smaller uncertainties for our measured $\sigma_{\rm n}$ relative to the analytical prediction could be explained by the additional information carried by narrow H β and [O III] λ5007 (7σ and 3σ detections, respectively), modulated by the presence of additional unknowns compared to the analytic approximation of L. Zhou et al. (2017), such as the absorber depth and redshift. We find no evidence of [N II] λ λ6548, 6583, with $F_{\rm n}$([N II]λ6583)/$F_{\rm n}$(H α) < 0.18 (3σ).

The flux ratio between the narrowest of the two broad Gaussians and the total broad H α is 0.45 ± 0.03. The width of the narrowest and broadest Gaussians are $FWHM = 560^{+50}_{-50}$ km s^{-1} and 2000^{+200}_{-100} km s^{-1}.

We perform a set of tests to establish whether our fiducial model is warranted, using the Bayes Information Criterion with a threshold Δ BIC > 10 as discriminant. A single Gaussian model to fit broad H α is ruled out, with Δ BIC > 30 (Appendix A). F. D'Eugenio et al. (2025) found mild asymmetry in the broad-line profile of the *Irony* LRD at $z = 6.68$, which they reproduce by decoupling the two broad Gaussians modelling broad H α. For Abell2744-QSO1, introducing independent velocity shifts $v_{\rm b,1}$ and $v_{\rm b,2}$ yields different centroids (-3^{+10}_{-9} and -110^{+40}_{-40} km s^{-1}, a 2.5σ difference) but no improvement over the fiducial model. We also tested decoupling the H β and H α broad lines, which also results in a fit that is indistinguishable from the fiducial model. Finally, we studied non-Gaussian line shapes, namely a Lorentzian profile (which may represent turbulent broadening; W. Kollatschny & M. Zetzl 2013, and which we parametrize as a Voigt profile, accounting for the finite instrument resolution), and a single Gaussian convolved with an exponential kernel (which may be due to Thomson scattering; A. Laor 2006; V. Rusakov et al. 2026). Both the Lorentzian and exponential-wings models provide an equally good fit as the fiducial model (Δ BIC $= 3$ in favour of the exponential-wings model). In Section 3.2, we discuss that these two alternative models are disfavoured based on the analysis of I. Juodžbalis et al. (2026a).

Table 1. Emission-line model of Abell2744-QSO1, reporting the median and 16th–84th percentile range of the posterior probability distribution for 18 free parameters of the model (Section 2; four free parameters for the continuum are not listed). The 'n' and 'b' subscripts denote values inherent to the narrow lines and to the (two-component) broad lines, respectively.

Observable	Value	Unit
$\mu F_{\rm n}$([O III]λ5007)[a]	$0.10^{+0.03}_{-0.03}$	10^{-18} erg s^{-1} cm^{-2}
$\mu F_{\rm n}$(H β)	$0.19^{+0.03}_{-0.02}$	10^{-18} erg s^{-1} cm^{-2}
$\mu F_{\rm n}$(H α)	$0.49^{+0.10}_{-0.08}$	10^{-18} erg s^{-1} cm^{-2}
$\mu F_{\rm n}$([N II]λ6583)	< 0.09	10^{-18} erg s^{-1} cm^{-2}
$\sigma_{\rm n}$	22^{+5}_{-6}	km s^{-1}
$z_{\rm n}$	$7.0366^{+0.0001}_{-0.0001}$	–
$v_{\rm b}$	-18^{+8}_{-8}	km s^{-1}
$F_{\rm b}$(H β)/$F_{\rm b}$(H α)	$0.11^{+0.01}_{-0.01}$	–
$\mu F_{\rm b}$(H α)	$13.9^{+0.9}_{-0.6}$	10^{-18} erg s^{-1} cm^{-2}
$F_{\rm b,1}/F_{\rm b}$(H α)	$0.45^{+0.03}_{-0.03}$	–
$FWHM_{\rm b,1}$(H α)[b]	560^{+50}_{-50}	km s^{-1}
$FWHM_{\rm b,2}$(H α)	2000^{+200}_{-100}	km s^{-1}
$v_{\rm abs,\,H\,\beta}$	50^{+20}_{-20}	km s^{-1}
$v_{\rm abs,H\,\alpha}$	-40^{+10}_{-10}	km s^{-1}
$\sigma_{\rm abs}$	110^{+20}_{-10}	km s^{-1}
C_f	$0.56^{+0.07}_{-0.07}$	–
τ_0(H β)	12^{+9}_{-5}	–
τ_0(H α)	$1.2^{+0.6}_{-0.3}$	–

Note.[a] The line fluxes are not corrected for lensing magnification nor for dust attenuation (see Table 2 for the corrected values). [b] The FWHM values reported here are model parameters for the two Gaussians representing the broad Balmer lines. The FWHM of the combined double-Gaussian profile is reported in Table 2.

3.1 Host galaxy

To estimate the dynamical mass of the system, we use the same approach as J25, but we leverage the higher spectral resolution and SNR of H α to infer a more accurate velocity dispersion $\sigma_{\rm n} = 22$ km s^{-1} of the gas. For the galaxy size, we adopt the upper limit on the half-light radius $R_{\rm e} < 30$ pc from L. J. Furtak et al. (2023). Our highest estimate of $M_{\rm dyn}$ is derived from the virial calibration of A. van der Wel et al. (2022), $M_{\rm dyn} = K(n)K(q)\sigma'^2_{\star,\rm int}R_{\rm sma}/G$, where $K(n)$ and $K(q)$ are functions of the Sérsic index n and the projected axis ratio q, $R_{\rm sma}$ is the semimajor axis and $\sigma'_{\star,\rm int}$ is the integrated stellar velocity dispersion. Assuming a Sérsic index $n = 1$ and axis ratio $q = 1$ leads to the highest possible value of the structural factor $K(n)K(q)$ in this calibration, hence the most conservative upper limit on $M_{\rm dyn}$ from the A. van der Wel et al.

Table 2. Summary of the derived parameters of Abell2744-QSO1, reporting the median and 16th–84th percentile range of the posterior probability distribution. All fluxes are corrected for dust redding, and all relevant quantities have been corrected for gravitational lensing magnification (assuming $\mu = 5.8$; L. J. Furtak et al. 2023). The 'n' and 'b' subscripts denote values inherent to the narrow lines and to the (two-component) broad lines, respectively.

Property	Posterior	Unit
$A_{V,\mathrm{n}}$	$-0.2^{+0.5}_{-0.5}$	mag
$A_{V,\mathrm{b}}$	$2.9^{+0.2}_{-0.2}$	mag
$F_{\mathrm{n}}(\mathrm{H}\,\beta)$	$0.03^{+0.02}_{-0.01}$	10^{-18} erg s^{-1} cm^{-2}<?vsp 2pt?>
$F_{\mathrm{n}}([\mathrm{O\,III}]\lambda5007)$	$0.013^{+0.011}_{-0.006}$	10^{-18} erg s^{-1} cm^{-2}
$F_{\mathrm{n}}(\mathrm{H}\,\alpha)$	$0.07^{+0.05}_{-0.03}$	10^{-18} erg s^{-1} cm^{-2}
$L_{\mathrm{n}}(\mathrm{H}\,\alpha)$	$0.04^{+0.03}_{-0.02}$	10^{42} erg s^{-1}
$SFR(\mathrm{H}\,\alpha)^{a}$	$0.7^{+0.4}_{-0.3}$	M$_\odot$ yr^{-1}
$EW_{\mathrm{abs}}(\mathrm{H}\,\beta)$	$9.0^{+0.6}_{-0.7}$	Å
$EW_{\mathrm{abs}}(\mathrm{H}\,\alpha)$	5^{+2}_{-1}	Å
$EW_{\mathrm{cont}}(\mathrm{H}\,\beta)$	11^{+3}_{-2}	Å
$EW_{\mathrm{b}}(\mathrm{H}\,\beta)$	-38^{+5}_{-6}	Å
$EW_{\mathrm{cont}}(\mathrm{H}\,\alpha)$	22^{+12}_{-7}	Å
$EW_{\mathrm{b}}(\mathrm{H}\,\alpha)$	-170^{+10}_{-20}	Å
$F_{\mathrm{b}}(\mathrm{H}\,\beta)$	$0.21^{+0.15}_{-0.09}$	10^{-18} erg s^{-1} cm^{-2}
$F_{\mathrm{b}}(\mathrm{H}\,\alpha)$	$2.1^{+0.9}_{-0.7}$	10^{-18} erg s^{-1} cm^{-2}
$FWHM_{\mathrm{b}}(\mathrm{H}\,\alpha)$	680^{+70}_{-80}	km s^{-1}
$\sigma_{\mathrm{l,b}}(\mathrm{H}\,\alpha)$	740^{+100}_{-120}	km s^{-1}
$\log M_\bullet^{\mathrm{RV15}}$	$6.3^{+0.1}_{-0.1}$	dex M$_\odot$
$\log M_\bullet^{\mathrm{DB25}}$	$6.5^{+0.1}_{-0.2}$	dex M$_\odot$
$\log M_\bullet$ (fiducial)	$7.2^{+0.1}_{-0.1}$	dex M$_\odot$
λ_{Edd}	$0.09^{+0.03}_{-0.02}$	–

Note.[a] This SFR assumes no AGN contribution, so should be regarded as an upper limit. [b] $\sigma_{\mathrm{l,b}}$ is the second moment of the observed line profile, as described in B. M. Peterson et al. (2004) and DB25. It shall not be confused with the dispersion of a Gaussian.

(2022) calibration. We also increase σ_{n} by 0.175 dex, following the calibration of R. Bezanson et al. (2018), as described in H. Übler et al. (2023) and R. Maiolino et al. (2024). This is meant to capture the different average value of σ between gas and stars (the latter of which underlies the calibration of A. van der Wel et al. 2022). However, we note that at low values of the stellar velocity dispersion, the calibration of R. Bezanson et al. (2018) may already implicitly capture an average inclination correction, since aperture velocity dispersion has a larger velocity contribution for gas than for stars (e.g. L. Cortese et al. 2016; D. Barat et al. 2019). Our inclusion of the R. Bezanson et al. (2018) scaling between the gas and stellar aperture dispersions thus yields an even more conservative upper limit on M_{dyn}, by 0.4 dex. With this approach, we find an upper limit $\log(M_{\mathrm{dyn}}/\mathrm{M}_\odot) < 8.0$. Alternatively, using the calibration of J. P. Stott et al. (2016) for purely dispersion dominated systems, we find $\log(M_{\mathrm{dyn}}/\mathrm{M}_\odot) < 7.1$. These are extremely low values, driven by the low dispersion of the narrow H α and by the unresolved nature of the galaxy in the spatial dimension.

We measure the Balmer decrement of the narrow lines from the total aperture, and find a dust attenuation value $A_{V,\mathrm{n}} = -0.2 \pm 0.5$ mag, fully consistent with no dust (Table 2), and possibly even suggesting an intrinsic line ratio lower than the standard Case-B value adopted here (W. McClymont et al. 2025a; G. P. Nikopoulos et al. 2025). The posterior chains include a dust attenuation correction, applied for every sample where $A_{V,\mathrm{n}} > 0$. For this, we adopted the K. D. Gordon et al. (2003) 'SMC-bar' dust extinction law and an intrinsic H α /H β flux ratio of 2.86, appropriate for Case-B recombination, electron temperature $T_{\mathrm{e}} = 10\,000$ K and density $n_{\mathrm{e}} = 500\,\mathrm{cm}^{-3}$.

For the BLR, assuming an intrinsic Balmer decrement of 3.1 (X. Dong et al. 2008), we find $A_{V,\mathrm{b}} = 2.9 \pm 0.2$ mag. We caution, however, that the intrinsic H α/H β ratio in BLRs is quite uncertain, reaching values up to 10 (D. Ilić et al. 2012). For Abell2744-QSO1, we disfavour such a high intrinsic ratio, because the observed Balmer decrement of the broad lines is also equal to 10 ± 1. Given this observed value, assuming an intrinsic decrement of 10 would imply little or no dust attenuation, at variance with the considerable dust found in front of the accretion disc ($A_V = 2.13 \pm 0.02$ mag; J25). On the other hand, other high-redshift LRDs seem to display non-Case-B ratios (G. P. Nikopoulos et al. 2025), and evidence for collisional excitation from a joint analysis of broad H γ , H β, and H α (F. D'Eugenio et al. 2025).

Based on the H α luminosity of the narrow component and using the star-formation rate (SFR) scaling of W. McClymont et al. (2025b), we infer $0.7^{+0.4}_{-0.3}\,\mathrm{M}_\odot\mathrm{yr}^{-1}$ (corrected for lensing using $\mu = 5.8$; L. J. Furtak et al. 2023). Using the calibration of A. E. Shapley et al. (2023), we would infer instead a much lower value of $0.09^{+0.05}_{-0.04}\,\mathrm{M}_\odot\mathrm{yr}^{-1}$. These values assume that the narrow-line region is completely dominated by star formation photoionization, with no AGN contribution. Clearly, since Abell2744-QSO1 is AGN dominated (J25), a more cautious approach would be to regard this SFR estimate as an upper limit. Following e.g. G. C. K. Leung et al. (2019), we can estimate the gas mass from the narrow-H α luminosity as

$$M_{\mathrm{H}\,\alpha} = 3.3 \times 10^{8}\mathrm{M}_\odot \frac{L_{\mathrm{n}}(\mathrm{H}\,\alpha)}{10^{43}\mathrm{erg\,s}^{-1}} \frac{100\mathrm{cm}^{-3}}{n_{\mathrm{e}}}, \quad (2)$$

where we assumed $T_{\mathrm{e}} = 10\,000$ K. For an electron density in the range 100–500 cm^{-3}, plausible for star-forming regions, we obtain an ionized-gas mass of 3-13 $\times$ 10^5 M$_\odot$, negligible relative to the dynamical masses. Higher densities such as those found in the absorber and in the BLR would further lower this estimate, but as we have seen, the small velocity dispersion of the narrow lines disfavours their origin too close to the BLR. Dark matter should also be negligible on these scales. For an object with $M_\star < M_{\mathrm{dyn}} < 10^{7.1}$-$10^{8}\mathrm{M}_\odot$, the halo mass at $z = 7$ should be of order $M_{\mathrm{h}} < 10^{10.9}$-$10^{11.3}$ M$_\odot$. Using the relations from J. S. Bullock et al. (2001) and A. A. Dutton & A. V. Macciò (2014), we can infer the scale density and scale radius, from which we derive the dark-matter mass inside the sphere of radius 30 pc to be $M_{\mathrm{h}}(R < 30\,\mathrm{pc}) < 3 \times 10^6$ M$_\odot$.

With the measured SFR, and using the upper limit on M_{dyn} as a limit on $M_\star$ too, we can relate this object to the star-forming main sequence of galaxies (SFMS). In Fig. 2, we show the position of Abell2744-QSO1 relative to star-forming galaxies at $z = 7.04$, from both observations and numerical simulations. Observational data are from the *JWST* Advanced Deep Extragalactic Survey (JADES; M. J. Rieke et al. 2023; K. N. Hainline et al. 2024; D. J. Eisenstein et al. 2026), where $M_\star$ and SFR were measured from spectral energy distribution (SED) modelling (C. Simmonds et al. 2024). Simulated galaxies are from the hydrodynamic suites DUSTYGADGET (L. Graziani et al. 2020; C. Di Cesare et al. 2023), THESAN-ZOOM (R. Kannan et al. 2025; W. McClymont et al. 2025b), and AESOPICA (S. Koudmani et al. 2022; Koudmani et al. in preparation). AESOPICA is a new suite of large-volume cosmological simulations (Koudmani et al. in preparation) built upon

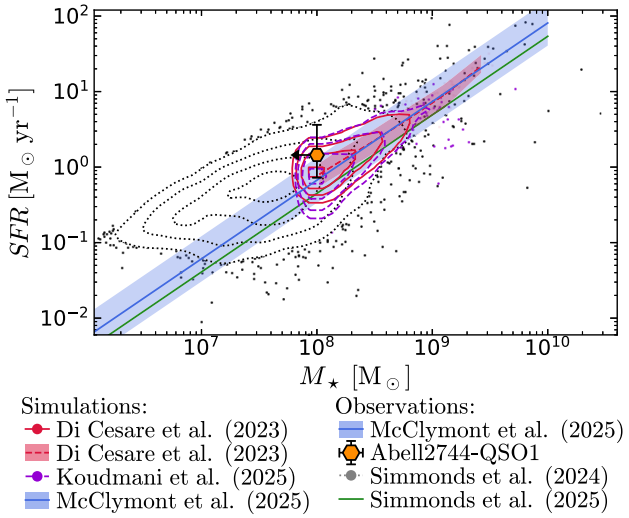

Figure 2. Abell2744-QSO1 in relation to the SFMS, using our largest upper limit on $M_{\rm dyn}$ as an upper limit on $M_\star$ too, and assuming that all the narrow Hα is due to star formation. Solid and dashed contours are simulated galaxies at z = 7-7.5 from DUSTYGADGET (L. Graziani et al. 2020; C. Di Cesare et al. 2023) and from AESOPICA (S. Koudmani et al. 2022; Koudmani et al. in preparation). The dashed red and solid-blue lines with shaded 0.2–0.3 dex scatter are the SFMS from the C. Di Cesare et al. (2023) and from the THESAN-ZOOM project (R. Kannan et al. 2025; W. McClymont et al. 2025b). The dotted contours are observed galaxies at $6.5 \leq z < 7.5$ from JADES (C. Simmonds et al. 2024), with the green line representing a bias-corrected SFMS model (C. Simmonds et al. 2025). Abell2744-QSO1 (orange hexagon) lies on the SFMS. Note that any AGN contribution to narrow Hα would lower the estimated SFR.

the FABLE galaxy formation model (N. A. Henden et al. 2018), with targeted updates for modelling the growth of infant SMBHs in the early Universe. AESOPICA explores three key modifications to fiducial galaxy formation models: enabling efficient accretion in the low-mass regime (S. Koudmani et al. 2022), incorporating super-Eddington accretion, and examining a broad range of seed masses ($10^2 M_\odot$ to $10^5 M_\odot$) following seed evolution from early cosmic epochs ($z \sim 20$).

Assuming that all the narrow Hα was due to star formation, we would infer a location of Abell2744-QSO1 on the SFMS, as inferred from all of DUSTYGADGET, THESAN-ZOOM, and AESOPICA. Clearly, an independent measure of the SFR is required to disentangle the AGN contribution, and to assess the precise star-forming nature of the host galaxy.

3.2 Black hole mass

To estimate the mass of the SMBH, we use two alternative virial calibrations, both based on the luminosity and width of the broad Hα line. The calibration of RV15 uses the line FWHM. In our case, we have three possible choices, depending on how the broad-line profile is interpreted. One could adopt the FWHM of the total line profile (modelled as the sum of two Gaussians), corrected for line absorption. With this method, and with $FWHM_{\rm b} = 680^{+70}_{-80}$ km s^{-1} (Table 2), we infer $\log(M_\bullet^{\rm RV15}/M_\odot) = 6.3^{+0.1}_{-0.1}$, with 0.3 dex additional uncertainty from the scatter about the calibration. These values are much lower than previous estimates based on the width of the broad Hβ line (L. J. Furtak et al. 2024; J25; FWHM$_{\rm b}$(Hβ) $= 2658^{+351}_{-292}$ km s^{-1}); the key difference is the much narrower FWHM of the *total* broad line profile (Table 2). Our total $FWHM_{\rm b}$(Hα) (Table 2) is much closer to the FWHM of the narrowest of the two broad Gaussians ($FWHM_{\rm b,1} = 560 \pm 50$ km s^{-1} versus $FWHM_{\rm b,2} = 2000^{+200}_{-100}$ km s^{-1}; Table 1), but this is a consequence of the flux ratio between the two components. Using instead the width of the broadest Gaussian, 2000^{+200}_{-100} km s^{-1}, one would infer $\log(M_\bullet^{\rm RV15}/M_\odot) = 7.2 \pm 0.1$. This measurement is in much better agreement with the Hβ -derived mass (L. J. Furtak et al. 2024; X. Ji et al. 2025).

As an alternative, we use a calibration based on the line second moment, $\sigma_{\rm l,b}$, which we measured on the observed line profile after subtracting the continuum. We remark that $\sigma_{\rm l,b}$ is not the dispersion of the Gaussian. In fact, we find $\sigma_{\rm l,b} = 740^{+100}_{-120}$ km s^{-1}, broader than $FWHM_{\rm b}$(Hα). This larger value is due to a combination of model assumptions (the $\sigma_{\rm l,b}$ method does not take into account the presence of the absorber) and to the broad wings of Hα , which are up-weighted when calculating the second-moment of the line profile. For reference, $\sigma_{\rm l,b}$ diverges for a Lorentzian-like line profile. From our estimate of $\sigma_{\rm l,b}$, using the calibration of DB25, we obtain $\log(M_\bullet^{\rm DB25}/M_\odot) = 6.5^{+0.1}_{-0.2}$, with 0.2 dex calibration uncertainties.

Crucially, the direct $M_\bullet$ measurement from I. Juodžbalis et al. (2026a) agrees best with the single-epoch virial estimate using the width of the broadest Gaussian component. Alternative estimates, such as from the FWHM of the sum of the two Gaussians, or from the line second moment, both fall significantly shorter than the direct measurement. The discrepancy between the dynamical estimate and the values inferred from the total profile can be understood if the narrowest of the two broad Gaussians is not related to the black-hole BLR. Evidence for a spatially resolved nature support a different physical origin of this kinematic component (I. Juodžbalis et al. 2026a).

Among the alternative models, both the Lorentzian/Voigt profile as well as the electron-scatter model (Appendix A) underpredict $M_\bullet$. In particular, the electron-scatter model of V. Rusakov et al. (2026) – coupled with the RV15 calibration – yields a value of $M_\bullet$ that is 1.7 dex below the dynamical estimate – despite this model being marginally better statistically than the fiducial model (Δ BIC = 5).

To obtain the bolometric luminosity, we use the calibration of J. Stern & A. Laor (2012), based on the broad Hα , and find $L_{\rm bol} = 2.1 \times 10^{44}$erg s^{-1}, within a factor of 2 from the value based on broad Hβ, as reported by J25.

3.3 Absorbing gas

The gas absorber has a very high equivalent width; when measured relative to the broad-Hα flux, the value is EW(Hα) $= 5^{+2}_{-1}$ Å, while the value measured relative to the continuum is $EW_{\rm cont}$(Hα) $= 22^{+12}_{-7}$ Å. Both values are very high, but the second value is so high that it completely rules out a stellar origin.[1] The strength of the Hβ absorber appears much larger, with an optical

[1] High-EW Balmer-line absorption in stellar atmospheres is routinely observed in spectral types from late B to early F, but is never as strong as seen here. For reference, for a simple stellar population employing MIST isochrones (J. Choi et al. 2016) and the C3K model atmospheres (C. Conroy et al. 2019), the maximum EW(Hα) is 8.3 Å for a burst age of 400–500 Myr, depending on metallicity. For Abell2744-QSO1, such an old burst age is ruled out by the amount of rest-UV light.

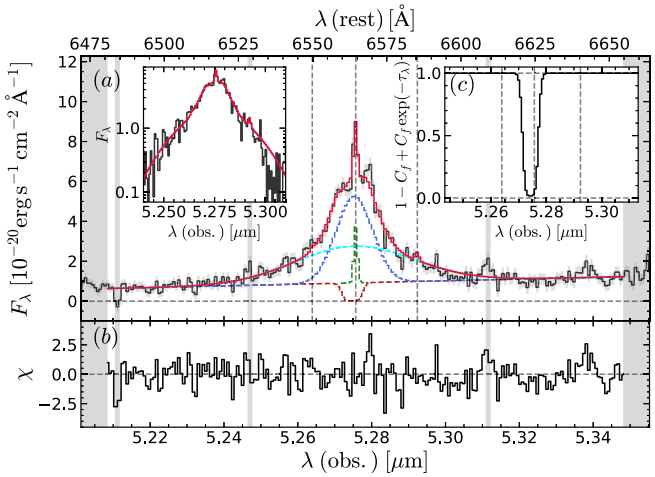

Figure 3. The best-fitting model where the dense gas absorbs only the continuum and not the broad H α line cannot reproduce the observations, therefore the dense absorber must be located between the observer and the BLR.

depth at the line centre of $\tau_0(\mathrm{H}\,\beta) = 12^{+9}_{-5}$, compared to only $\tau_0(\mathrm{H}\,\alpha) = 1.2^{+0.6}_{-0.3}$. Since these are absorption lines arising from the same energy level, their optical depth ratios are set by atomic physics to be $\tau_0(\mathrm{H}\,\beta)/\tau_0(\mathrm{H}\,\alpha) = \lambda_{\mathrm{H}\,\beta}/\lambda_{\mathrm{H}\,\alpha} \cdot f_{2\to4}/f_{2\to3} = 0.137$, where we used the oscillator strength values $f_{2\to4} = 0.119$ and $f_{2\to3} = 0.641$. Our results yield $\tau_0(\mathrm{H}\,\beta)/\tau_0(\mathrm{H}\,\alpha) = 10 \pm 6$, almost 2σ away from the theoretical value. Higher-quality observations of H β are needed to confirm this finding in Abell2744-QSO1, but similar results have been reported for other LRDs (F. D'Eugenio et al. 2026, 2025), lending credibility to this low-SNR result. Additionally, the H β and H α absorber require two different velocities, with $v_{\mathrm{abs,H}\,\beta} - v_{\mathrm{abs,H}\,\alpha} = 90 \pm 30\,\mathrm{km\,s^{-1}}$. Again, while this is only a 3σ result, other LRDs have been confirmed to have different H α and H β absorber velocities (F. D'Eugenio et al. 2025; X. Ji et al. 2026; X. Lin et al. 2026). At face value, the kinematic discrepancy in the two absorbers suggests the presence of some line infill, possibly P-cygni profiles (A. Torralba et al. 2025; V. Rusakov et al. 2026). Spatially, the absorber is clearly located in the BLR, or between the BLR and the observer, as demonstrated in Fig. 3; there is clearly not enough continuum flux to be absorbed, and the model is unable to reproduce the data.

The mean velocity offset of the BLR model is $v_{\mathrm{b}} = -18 \pm 8\,\mathrm{km\,s^{-1}}$. This is only a 2.5σ difference, so we do not regard it as strong evidence for a velocity offset, especially since we miss the peak of the BLR due to the absorption. The velocity of the H α absorber is also very close to the systemic velocity, $v_{\mathrm{abs}} = -40 \pm 10\,\mathrm{km\,s^{-1}}$. This weak blueshift echoes the blueshift of the BLR, such that their difference $22 \pm 13\,\mathrm{km\,s^{-1}}$ is fully consistent with zero (within 1.7σ), implying that the dense-gas absorber is at or very near rest-frame velocity relative to the BLR.

While a single rest-frame absorber could indicate an inflow/outflow directed close to the plane of the sky, there is increasing evidence for near rest-frame absorbers being common (e.g. F. D'Eugenio et al. 2025, 2026; Y. Ma et al. 2025a), favouring stationary equilibrium, such as a gas disc, or at least long-lived structures, such as stalling gas clouds. Indeed, if we adopt the column density $N_{\mathrm{H}} \sim 10^{24}\mathrm{cm^{-2}}$ estimated from the strength of the Balmer absorption (J25), the gas absorber could be long-lived even under a high-λ_{Edd} scenario, because the cross section for absorption depends on the dust fraction (A. C. Fabian, R. V. Vasudevan & P. Gandhi 2008), which we estimate to be low. In fact, from the dust-to-column density ratio of the Milky Way (MW) and from the hydrogen column density of J25, we can derive constraints on the dust and metallicity properties of the absorbing gas. Following the method of F. D'Eugenio et al. (2024b, their equation 1), we can write

$$Z \times \xi_{\mathrm{d}} = Z_{\mathrm{MW}} \times \xi_{d,MW} \frac{A_{V,\mathrm{n}}}{N_{\mathrm{H}}} \left(\frac{N_{\mathrm{H}}}{A_V}\right)_{\mathrm{MW}}, \quad (3)$$

where Z is the ISM metallicity, ξ_{d} is the dust-to-metal ratio. Adopting the MW values of the gas-to-extinction ratio $N_{\mathrm{H}}/A_V = (2.09 \pm 0.03) \times 10^{21}\mathrm{cm^{-2}\,mag^{-1}}$ (H. Zhu et al. 2017), the dust-to-metal ratio $\xi_{\mathrm{d,MW}} = 0.45$ (C. Konstantopoulou et al. 2024), and an ISM metallicity in the solar neighbourhood $Z_{\mathrm{MW}} = 0.6\,\mathrm{Z_\odot}$ (K. Z. Arellano-Córdova et al. 2021), and using a 3σ upper limit on the dust content of $A_{V,\mathrm{n}} < 1.5$ mag, we infer $Z \cdot \xi_{\mathrm{d}} \lesssim 0.0008\,\mathrm{Z_\odot}$. The inequality stems from the upper limit on $A_{V,\mathrm{n}}$, but one must recall that even if dust was detected, some or even most of the narrow-line attenuation may not be associated with the absorber. At face value, such a low $Z \cdot \xi_{\mathrm{d}}$ implies that the absorbing medium is extremely dust poor. This could stem in part from a very low value of ξ_{d}, which would be expected if the absorber is within the dust sublimation radius from the SMBH, and in part from intrinsically low metallicity – which resonates with the emission-line analysis of R. Maiolino et al. (2025a), who use the narrow-line ratios to estimate $Z_{\mathrm{gas}} < 0.01\mathrm{Z_\odot}$. Whatever the reason (absence of metals or dust sublimation), our estimate of $Z \cdot \xi_{\mathrm{d}}$ would lower the effective Eddington ratio for the galaxy interstellar medium (ISM), thus increasing the lifetime of absorbing clouds (A. C. Fabian et al. 2008; N. Arakawa et al. 2022).

4 DISCUSSION

LRDs defined as having broad permitted lines, a 'v-shaped' SED, and very compact morphology, are a puzzling new class of AGN, unknown before *JWST*. It is clear that these objects are preferentially found in the Universe before Cosmic Noon, at $z >$ 2-3 (Y. Ma et al. 2025a; X. Lin et al. 2026).

Abell2744-QSO1 (L. J. Furtak et al. 2023, 2024) was found to have one of the strongest Balmer breaks observed at high redshift (see also I. Labbe et al. 2024). The smooth nature of the break in this galaxy has defied any attempt to model it as a stellar Balmer break (Y. Ma et al. 2025b). In contrast, by using the model of K. Inayoshi & R. Maiolino (2025), which associates the Balmer break to dense gas absorbers around the AGN, and by introducing a large micro-turbulence parameter of $v_{\mathrm{t}} \sim 120\,\mathrm{km\,s^{-1}}$, J25 were able to successfully model the shape of the continuum break.

4.1 Properties of the gas absorber

One of the key predictions of the K. Inayoshi & R. Maiolino (2025) model is the presence of high-EW Balmer-line absorption. While J25 reported tentative evidence of H β absorption, the much higher SNR of the H α emission line enables us not only to confirm beyond any doubt that Abell2744-QSO1 also has H α absorption (Fig. 1), but also to study its kinematics. The EW of this absorption is too large to be of stellar origin, completely ruling out a stellar-atmosphere interpretation of the Balmer break. The inferred broadening, $\sigma_{\mathrm{abs}} = 110^{+20}_{-10}\,\mathrm{km\,s^{-1}}$, closely matches the micro-turbulence value required to model the continuum shape (by definition $v_{\mathrm{t}} \equiv \sqrt{2}\sigma_{\mathrm{abs}}$). Such a high degree of smoothness cannot be obtained from stellar atmospheres ($v_{\mathrm{turb}} \lesssim 15\,\mathrm{km\,s^{-1}}$;

K. C. Smith & I. D. Howarth 1998), or from stellar kinematics (given the Gaussian dependence of kinematics-driven broadening, while turbulence-driven broadening is exponential).

Different aspects of our analysis favour a location of the absorber within or just outside the BLR. First, because the absorption is too deep to absorb only the continuum (in agreement with the 'Rosetta Stone' LRD from I. Juodžbalis et al. 2024a). Second, the density of the absorber is fully consistent with the high densities of BLRs (J25).

4.2 Absorber energetics

The high value of the turbulence (now coming from two independent measurements) must indicate either a transient nature, or an adequate energy source to counteract dissipation, which for turbulent energy is of order of the crossing time (M.-M. Mac Low 1999; M.-M. Mac Low & R. S. Klessen 2004; R. S. Klessen & S. C. O. Glover 2016). Since we do not know the scale of the turbulent motions, we can derive an upper limit to the dissipation time by using the size of the system, hence the dissipation time must be shorter than $30\,\mathrm{pc}/(110\,\mathrm{km\,s^{-1}}) \sim 200\,000$ yr. We can obtain a crude estimate of the clouds turbulent-energy density from the usual definition of kinetic energy, as $1.4 m_\mathrm{p} n_\mathrm{H} \cdot \sigma^2_\mathrm{abs}$, with $n_\mathrm{H} = 10^{8.5}$-$10^{10}\mathrm{cm^{-3}}$ (J25). Using simple geometry, a spherical shell of radius R_c, thickness δR_c and solid angle Ω_c has total turbulent energy

$$E_\mathrm{c} = 6.9\times10^{50}\left(\frac{\Omega_\mathrm{c}}{4\pi}\right)\left(\frac{n_\mathrm{H}}{10^8\mathrm{cm^{-3}}}\right) \left(\frac{R_\mathrm{c}}{1\mathrm{pc}}\right)^2\left(\frac{\delta R_\mathrm{c}}{0.001\mathrm{pc}}\right)\left(\frac{\sigma_\mathrm{abs}}{100\mathrm{km\,s^{-1}}}\right)^2 \mathrm{erg}. \quad (4)$$

For the galactocentric distance of the clouds R_c we use the size of the BLR; since there is not enough continuum to be absorbed (Section 3.3), the clouds must be back-illuminated by the BLR, at least in part. We set therefore a lower limit $R_\mathrm{c} = R_\mathrm{BLR} > 2.7$ pc, where the lower bound on the size of the BLR has been derived from the time delay between the continuum and emission-line variability (J25). The thickness of the clouds is not known for the object in hand, but it has been estimated to be $\delta R_\mathrm{c} < 10^{-3}$ pc in a low-redshift LRD (I. Juodžbalis et al. 2024a). With these numbers and setting $\Omega_\mathrm{c} = 4\pi$, the turbulent energy of the absorbing clouds is $E_\mathrm{c} \sim 10^{52}$-$10^{53}$ erg. Under the assumption of a long-lived cloud, we can estimate the power required to maintain the turbulence as $P_\mathrm{c} \sim E_\mathrm{c}/(\delta R_\mathrm{c}/\sigma_\mathrm{abs})$, or

$$P_\mathrm{c} = 2.2\times10^{42}\left(\frac{\Omega_\mathrm{c}}{4\pi}\right)\left(\frac{n_\mathrm{H}}{10^8\mathrm{cm^{-3}}}\right) \left(\frac{R_\mathrm{c}}{1\mathrm{pc}}\right)^2\left(\frac{\sigma_\mathrm{abs}}{100\mathrm{km\,s^{-1}}}\right)^3 \mathrm{erg\,s^{-1}}, \quad (5)$$

which are comparable to the bolometric luminosity of the AGN, $L_\mathrm{bol} \sim 10^{44}\mathrm{erg\,s^{-1}}$.

The outcome of the previous estimates depends on two very uncertain assumptions. The large-scale covering factor of the dense absorbers, and the turbulence decay time, $\delta R_\mathrm{c}/\sigma_\mathrm{abs}$. Based on the fraction of LRDs with confirmed line absorption, it is reasonable to estimate $\Omega_\mathrm{c}/(4\pi) > 0.1$, which would imply that the absorbing clouds are an important component of the energy budget in LRD AGN. For the turbulence decay time, we have assumed the smallest physical size of the clouds. However, since the resulting crossing time is only of order 10 yr, it is difficult to imagine these clouds being long lived, which is required to explain the relatively high fraction of LRDs with absorption. It is thus possible that the absorbing gas constitutes the limiting edge of the Strömgren sphere, and that it is therefore contiguous to higher ionization gas, perhaps the BLR itself. In this case, the decay time would be significantly longer, depending on the actual scale of the turbulence. Alternatively, the observed σ_abs may represent a velocity dispersion between different clouds, but in this case we would expect significant cloud–cloud collisions. Still, a dynamical environment, where absorbing clouds are continuously formed and destroyed on short time-scales is also possible, and it is supported by observations of gas absorption in local AGN (R. Maiolino et al. 2010, although, in the latter case, the absorption is much weaker).

4.3 Black hole mass and Eddington accretion rate

Using the total line width of $FWHM_\mathrm{b} = 680^{+70}_{-80}\,\mathrm{km\,s^{-1}}$, the estimated $M_\bullet$ would be roughly one order of magnitude lower than previous values based on Hβ . However, this result would be in strong contradiction with I. Juodžbalis et al. (2026a), who measure $M_\bullet$ by combining dynamical modelling of the resolved narrow Hα and spectroastrometry, finding $\log(M_\bullet/\mathrm{M_\odot}) = 7.7$. This result is in much better agreement with the estimate from the width of the broadest Hα component, which – applying the RV15 calibration – is 7.2 ± 0.1.

All alternative choices of model or line width yield much lower $M_\bullet$ values. Specifically, the non-parametric line width calibration of E. Dalla Bontà et al. (2025) yields $\log(M_\bullet/\mathrm{M_\odot}) = 6.5$ – despite this calibration having the lowest scatter. A possible explanation is that the intermediate-width component (which is spatially resolved; I. Juodžbalis et al. 2026a) may not be associated with the BLR, and should be subtracted before measuring $\sigma_\mathrm{l,b}$.

Using a Lorentzian/Voigt profile yields similar results as using the total line width from the sum of the two Gaussians (Appendix A). Similarly, the electron scattering scenario also yields much lower $M_\bullet$.

Our high $M_\bullet$ results in a low Eddington ratio. With the bolometric luminosity estimated from Hα (or, equivalently, from the optical continuum, J25), we infer a sub-Eddington accretion rate, $\lambda_\mathrm{Edd} = 0.09$.

Our higher SNR and spectral resolution reduce the dynamical mass of the whole system to the range $\log(M_\mathrm{dyn}/\mathrm{M_\odot}) = 7.1{-}8.0$ (depending on the calibration adopted). With these values, we obtain a range of $M_\bullet/M_\mathrm{dyn}$ between 0.15 and 1.2, indicating an overmassive black hole, and reaching the regime where the black-hole dominates the entire system (in agreement with X. Ji et al. 2025 and I. Juodžbalis et al. 2026a). These values indicate a strong deviation not only from the $M_\bullet$–$M_\star$ relation, but even from the $M_\bullet$–σ relation (R. Maiolino et al. 2024), suggesting a departure from the co-evolution path (J25), possibly associated with a black hole-first scenario. Analysis of black-hole evolutionary tracks in scenarios where $z \sim 4$ overmassive black holes grow through short phases of super-Eddington accretion suggests that they tend to grow independently of their final host galaxy (in independent progenitor halos) down to $z \sim 8$, and start 'co-evolving' only thereafter (A. Trinca et al. 2024). Before that, their BH to stellar mass ratio may be even more extreme than observed at $z \sim 5$, possibly matching a system as extreme as Abell2744-QSO1.

The largest uncertainty on these ratios derives from the galaxy virial calibrations, which span one dex in M_dyn. In Fig. 4(a), we show the $M_\bullet$–$M_\star$ relation, where we use our most conservative

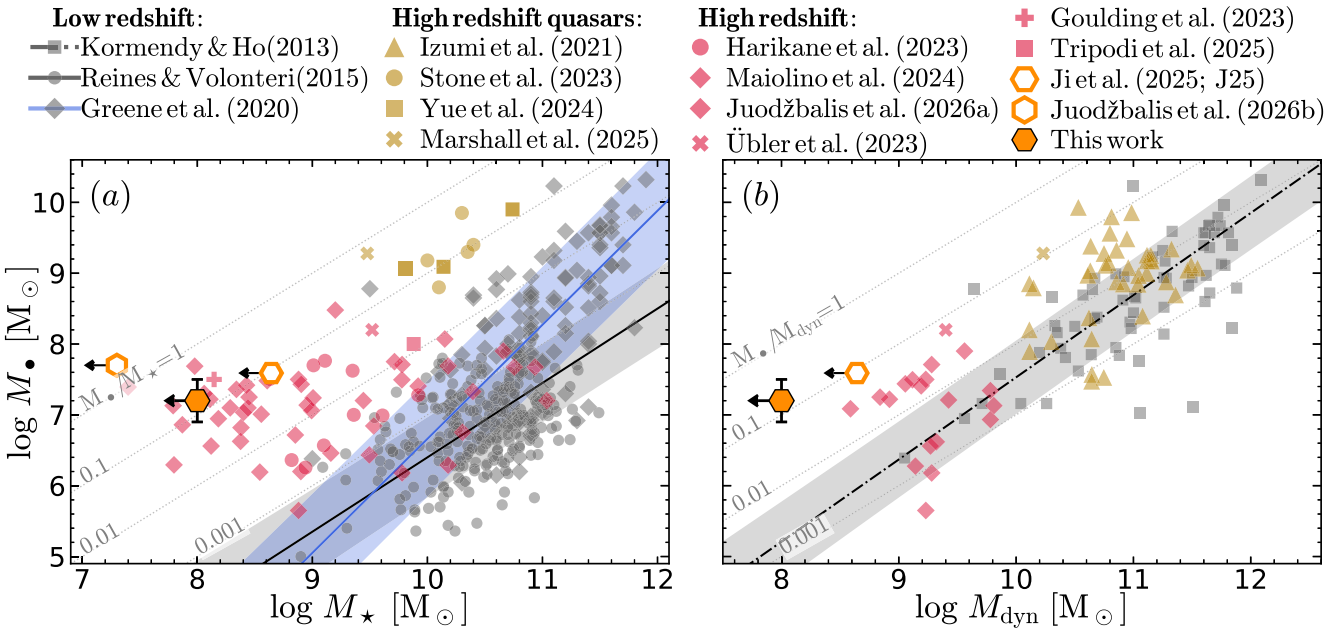

Figure 4. Using our fiducial determination of $M_\bullet$ from the width of the broadest Gaussian, Abell2744-QSO1 (filled orange hexagon) is overmassive relative to both $M_\star$ (panel a) and $M_{\rm dyn}$ (panel b), when compared to local scaling relations, similar to other *JWST*-discovered AGN (red symbols). Our estimates based on H α revise both $M_\bullet$ and $M_{\rm dyn}$ down relative to the H β and [O III] λ5007 estimates, though $M_\bullet$ is up to 0.5-dex lower than the H β and direct estimates (empty hexagons; J25, I. Juodžbalis et al. 2026a). The main conclusion that Abell2744-QSO1 is overmassive remains unchanged. The local scaling relations are from J. Kormendy & L. C. Ho (2013), RV15, and J. E. Greene, J. Strader & L. C. Ho (2020). High-redshift quasars are from T. Izumi et al. (2021), M. A. Stone et al. (2023), M. Yue et al. (2024), and M. A. Marshall et al. (2025). High-redshift, low-luminosity AGN are from Y. Harikane et al. (2023), H. Übler et al. (2023), A. D. Goulding et al. (2023), R. Maiolino et al. (2024), R. Tripodi et al. (2025), and I. Juodžbalis et al. (2026b).

upper limit on $M_{\rm dyn}$ as an upper limit on $M_\star$ too; despite revising $M_\bullet$ down, we confirm that the SMBH in Abell2744-QSO1 makes up at least 15 per cent of the stellar mass.

In Fig. 4(b) we compare our new measurements to local scaling relations between $M_\bullet$ and $M_{\rm dyn}$, and confirm the overmassive nature of the SMBH in Abell2744-QSO1. In any case, regardless of the $M_\bullet$ and $M_{\rm dyn}$ adopted, the SMBH is a dominant component of the dynamics of this system, with a sphere of influence of 18–45 pc, which is comparable to or even larger than the upper limit on $R_{\rm e}$ (I. Juodžbalis et al. 2026a).

The observation of turbulent gas absorbers consistent with rest-frame velocities, together with their low dust (and metallicity; J25) content and with low $\lambda_{\rm Edd}$ ratios, suggests a scenario where accreted gas is piled up in a dense reservoir near the black hole, giving rise to long-lived absorption (A. C. Fabian et al. 2008).

Since dense $n = 2$ absorbers are rare in normal AGN (R. Maiolino et al. 2025b), accretion or black-hole feedback should normally be able to clear this gas. However, several conditions in the early Universe may favour gas accumulation. Accreting gas at early times would naturally have low angular momentum (since low-angular momentum gas would collapse earlier and more efficiently; e.g. A. Renzini 2025), leading to a high accretion rate towards the innermost regions of proto-galaxies, where massive black holes dominate the gravitational potential. The compact nature of LRDs naturally agrees with a low-angular-momentum budget (A. Loeb 2024; F. Pacucci & A. Loeb 2025), and the high black-hole to total mass fraction supports scenarios of black-hole dominated galaxies (J25).

While radiation pressure would push the gas outwards, high gas density, metals, and dust just outside the sublimation zone would favour gas cooling. At the same time, the very low metallicity and dust content of newly accreted gas mean that its coupling to the accretion-disc radiation is essentially driven by the Thomson cross-section, not by dust absorption. This is different from later epochs and from more evolved galaxies, where dust in the ISM increases the coupling with radiation up to 10- or 100-fold relative to the Thomson cross-section (A. C. Fabian et al. 2008). If this gas is stalling due to weak radiation pressure, it would naturally have a high degree of turbulence, but negligible radial velocity, consistent with observations. Its accumulation would lead to high covering factors, also consistent with observations.

In this scenario, the SMBH would be unable to regulate gas accretion onto the galaxy (F. Pacucci & R. Narayan 2024), explaining why the $M_\bullet$–$M_\star$ relation does not hold for proto-galaxies at $z \gtrsim 5$ (Y. Harikane et al. 2023; R. Maiolino et al. 2024), but why it is in place at lower redshifts and for more massive, more evolved galaxies (Y. Sun et al. 2025). Indeed, at later epochs, metal dissemination from the first galaxies and higher angular momentum would lead to larger galaxies, where the impact of the central SMBH on the gravitational potential of the host galaxy becomes negligible (except for the innermost regions), but where its ability to regulate the galaxy ISM increases dramatically. This evolution would naturally explain the disappearance of LRDs at later epochs, which currently seems to largely occur by $z \sim 2$ (I. Juodžbalis et al. 2024a; Y. Ma et al. 2025a), although a few rare cases have been discovered at $z = 0.1$-0.2 (X. Lin et al. 2026; X. Ji et al. 2026).

5 CONCLUSIONS

In this work, we present $R = 3,700$ *JWST* NIRSpec/IFS aperture spectroscopy of the H α line in the broad-line AGN Abell2744-

QSO1 at $z = 7.04$. Leveraging the higher SNR of these data, we find

(i) The H α emission line consists of a narrow-line component (6σ detection) and a broad-line component. The latter has distinctively non-Gaussian line profile with observed $FWHM = 680^{+70}_{-80}$ km s^{-1}.

(ii) From the Balmer decrement of the narrow lines, we infer $A_V = -0.2 \pm 0.5$ mag, consistent with no dust. Interpreting the narrow H α line as solely due to star formation, we infer a delensed SFR of $0.7^{+0.4}_{-0.3}$ M$_\odot$yr^{-1}.

(iii) Our revised SMBH mass is $\log(M_\bullet/\mathrm{M}_\odot) = 7.2$, derived from the width of the broadest Gaussian and from the RV15 calibration.

(iv) Assuming local calibrations for the bolometric AGN luminosity, we infer Eddington ratios $\lambda_{\rm Edd} = 0.09$.

(v) The narrow line has an intrinsic $\sigma_{\rm n} = 22^{+5}_{-6}$ km s^{-1}. The resulting $M_{\rm dyn}$ is $\log(M_{\rm dyn}/\mathrm{M}_\odot) = 7.1$-$8.0$, implying very high $M_\bullet/M_{\rm dyn} = 0.15$-$1.2$.

(vi) Broad H α is subject to foreground hydrogen Balmer-line absorption with high EW and large broadening $\sigma_{\rm abs} = 110^{+20}_{-10}$ km s^{-1}, which rules out a stellar origin. This detection confirms the predictions of K. Inayoshi & R. Maiolino (2025) and J25 of a link between AGNs with Balmer breaks and Balmer-line absorption. Our $\sigma_{\rm abs}$ is consistent with the micro-turbulence inferred from independent modelling of the Balmer break by J25.

(vii) The H α absorber has low line-of-sight velocity, consistent with the velocity of the broad H α emission line and is very close to the velocity of the narrow lines, implying that the absorbing gas cannot be interpreted as an inflow or outflow.

(viii) Comparing the column density and ISM attenuation of the galaxy, we infer that the $n = 2$ absorber is dust poor.

Our findings confirm the overmassive nature of the SMBHs in low-luminosity, 'LRD' AGNs. The overmassive nature of Abell2744-QSO1 suggests intriguing possibilities regarding the formation of early SMBHs, such as SMBHs dominating the gravitational potential, and large supply of cosmic gas that can be efficiently fuelled onto SMBHs leading to rapid growth.

ACKNOWLEDGEMENTS

We thank the anonymous referee for their constructive report. We are grateful to Claudia Di Cesare for sharing the DUSTYGADGET results. FDE, RM, GCJ, XJ, WM, and JS acknowledge support by the Science and Technology Facilities Council (STFC), by the ERC through Advanced Grant 695671 'QUENCH', and by the UKRI Frontier Research grant RISEandFALL. RM also acknowledges funding from a research professorship from the Royal Society. GM acknowledges financial support from the grant PRIN MIUR 2017PH3WAT ('Black hole winds and the baryon life cycle of galaxies'). SA acknowledges grant PID2021-127718NB-I00 funded by the Spanish Ministry of Science and Innovation/State Agency of Research (MICIN/AEI/10.13039/501100011033) SC and GV acknowledge support by European Union's HE ERC Starting Grant No. 101040227 - WINGS. MVM was supported by the National Science Foundation via AAG grant 2205519, the Wisconsin Alumni Research Foundation via grant MSN251397, and NASA via STScI grant JWST-GO-4426. AJB acknowledges funding from the 'First-Galaxies' Advanced Grant from the European Research Council (ERC) under the European Union's Horizon 2020 research and innovation program (Grant agreement No. 789056). ST acknowledges support by the Royal Society Research Grant G125142. CT acknowledges support from STFC grants ST/R000964/1 and ST/V000853/1. HÜ acknowledges funding by the European Union (ERC APEX, 101164796). Views and opinions expressed are however those of the authors only and do not necessarily reflect those of the European Union or the European Research Council Executive Agency. Neither the European Union nor the granting authority can be held responsible for them. MP acknowledges grant PID2021-127718NB-I00 funded by the Spanish Ministry of Science and Innovation/State Agency of Research (MICIN/AEI/ 10.13039/501100011033), and the grant RYC2023-044853-I, funded by MICIU/AEI/10.13039/501100011033 and European Social Fund Plus (FSE+).

This work made extensive use of the freely available Debian GNU/Linux operating system. We used the Python programming language (G. van Rossum 1995), maintained and distributed by the Python Software Foundation. We made direct use of PYTHON packages ASTROPY (Astropy Collaboration 2013), CORNER (D. Foreman-Mackey 2016), EMCEE (D. Foreman-Mackey et al. 2013), JWST (C. Alves de Oliveira et al. 2018), MATPLOTLIB (J. D. Hunter 2007), NUMPY (C. R. Harris et al. 2020), and SCIPY (E. Jones et al. 2001). We also used the software TOPCAT (M. B. Taylor 2005), FITSMAP (R. Hausen & B. E. Robertson 2022), and DS9 (W. A. Joye & E. Mandel 2003).

DATA AVAILABILITY

This work is based on observations made with the NASA/ESA/CSA *James Webb Space Telescope*. The data were obtained as part of *JWST* programme ID 5015, and are available from the Mikulski Archive for Space Telescopes at the Space Telescope Science Institute, which is operated by the Association of Universities for Research in Astronomy, Inc., under NASA contract NAS 5-03127 for *JWST*. The extended-wavelength extracted spectrum is available on zenodo, DOI: 10.5281/zenodo.18548692.

REFERENCES

Alves de Oliveira C. et al., 2018, preprint (arXiv:1805.06922)
Arakawa N., Fabian A. C., Ferland G. J., Ishibashi W., 2022, MNRAS, 517, 5069
Arellano-Córdova K. Z., Esteban C., García-Rojas J., Méndez-Delgado J. E., 2021, MNRAS, 502, 225
Astropy Collaboration, 2013, A&A, 558, A33
Baggen J. F. W. et al., 2024, ApJ, 977, L13
Barat D. et al., 2019, MNRAS, 487, 2924
Bechtold K., Böker T., Franz D. E., te Plate M., Rawle T. D., Wu R., Zeidler P., 2024, preprint (arXiv:2408.15940)
Begelman M. C., Volonteri M., Rees M. J., 2006, MNRAS, 370, 289
Bezanson R. et al., 2018, ApJ, 868, L36
Böker T. et al., 2022, A&A, 661, A82
Bromm V., Loeb A., 2003, Nature, 425, 812
Bullock J. S., Kolatt T. S., Sigad Y., Somerville R. S., Kravtsov A. V., Klypin A. A., Primack J. R., Dekel A., 2001, MNRAS, 321, 559
Carnall A. C. et al., 2023, Nature, 619, 716
Chabrier G., 2003, PASP, 115, 763
Choi J., Dotter A., Conroy C., Cantiello M., Paxton B., Johnson B. D., 2016, ApJ, 823, 102
Conroy C., Naidu R. P., Zaritsky D., Bonaca A., Cargile P., Johnson B. D., Caldwell N., 2019, ApJ, 887, 237
Cortese L. et al., 2016, MNRAS, 463, 170
D'Eugenio F. et al., 2024a, Nat. Astron., 8, 1443
D'Eugenio F. et al., 2024b, A&A, 689, A152

D'Eugenio F. et al., 2025, preprint (arXiv:2510.00101)
D'Eugenio F. et al., 2026, MNRAS, 545, staf2117
Dalla Bontà E. et al., 2025, A&A, 696, A48 (DB25)
Di Cesare C., Graziani L., Schneider R., Ginolfi M., Venditti A., Santini P., Hunt L. K., 2023, MNRAS, 519, 4632
Dojčinović I., Kovačević-Dojčinović J., Popović L. Č., 2023, Adv. Space Res., 71, 1219
Dong X., Wang T., Wang J., Yuan W., Zhou H., Dai H., Zhang K., 2008, MNRAS, 383, 581
Dubois Y., Volonteri M., Silk J., Devriendt J., Slyz A., Teyssier R., 2015, MNRAS, 452, 1502
Dutton A. A., Macciò A. V., 2014, MNRAS, 441, 3359
Eisenstein D. J. et al., 2026, ApJS, 283, 6
Fabian A. C., 2012, ARA&A, 50, 455
Fabian A. C., Vasudevan R. V., Gandhi P., 2008, MNRAS, 385, L43
Ferrarese L., Merritt D., 2000, ApJ, 539, L9
Ferruit P. et al., 2022, A&A, 661, A81
Fiore F. et al., 2017, A&A, 601, A143
Foreman-Mackey D., 2016, J. Open Source Softw., 1, 24
Foreman-Mackey D., Hogg D. W., Lang D., Goodman J., 2013, PASP, 125, 306
Furtak L. J. et al., 2023, ApJ, 952, 142
Furtak L. J. et al., 2024, Nature, 628, 57
Furtak L. J. et al., 2025, A&A, 698, A227
Gebhardt K. et al., 2000, ApJ, 539, L13
Gordon K. D., Clayton G. C., Misselt K. A., Landolt A. U., Wolff M. J., 2003, ApJ, 594, 279
Goulding A. D. et al., 2023, ApJ, 955, L24
Graziani L., Schneider R., Ginolfi M., Hunt L. K., Maio U., Glatzle M., Ciardi B., 2020, MNRAS, 494, 1071
Greene J. E., Strader J., Ho L. C., 2020, ARA&A, 58, 257
Greene J. E. et al., 2024, ApJ, 964, 39
Hainline K. N. et al., 2024, ApJ, 964, 71
Harikane Y. et al., 2023, ApJ, 959, 39
Harris C. R. et al., 2020, Nature, 585, 357
Hausen R., Robertson B. E., 2022, Astron. Comput., 39, 100586
Henden N. A., Puchwein E., Shen S., Sijacki D., 2018, MNRAS, 479, 5385
Horne K., 1986, PASP, 98, 609
Hunter J. D., 2007, Comput. Sci. Eng., 9, 90
Ilić D., Popović L. Č., La Mura G., Ciroi S., Rafanelli P., 2012, A&A, 543, A142
Inayoshi K., Maiolino R., 2025, ApJ, 980, L27
Inayoshi K., Visbal E., Haiman Z., 2020, ARA&A, 58, 27
Izumi T. et al., 2021, ApJ, 914, 36
Jakobsen P. et al., 2022, A&A, 661, A80
Ji X. et al., 2025, MNRAS, 544, 3900 (J25)
Ji X. et al., 2026, MNRAS, 545, staf2235
Jones E., Oliphant T., Peterson P. et al., 2001, http://www.scipy.org/ (Accessed 2026-03-23)
Jones G. C. et al., 2026, MNRAS, 546, stag115
Joye W. A., Mandel E., 2003, in Payne H. E., Jedrzejewski R. I., Hook R. N., eds, ASP Conf. Ser. Vol. 295, Astronomical Data Analysis Software and Systems XII. Astron. Soc. Pac., San Francisco, p. 489
Juodžbalis I. et al., 2024a, MNRAS, 535, 853
Juodžbalis I. et al., 2024b, Nature, 636, 594
Juodžbalis I. et al., 2026a, preprint (arXiv:2508.21748)
Juodžbalis I. et al., 2026b, MNRAS, 546, stag086
Kannan R. et al., 2025, Open J. Astrophys., 8, 153
Klessen R. S., Glover S. C. O., 2016, Saas-Fee Advanced Course, 43, 85
Kocevski D. D. et al., 2023, ApJ, 954, L4
Kokorev V. et al., 2023, ApJ, 957, L7
Kokubo M., Harikane Y., 2025, ApJ, 995, 24
Kollatschny W., Zetzl M., 2013, A&A, 549, A100
Konstantopoulou C. et al., 2024, A&A, 681, A64
Kormendy J., Ho L. C., 2013, ARA&A, 51, 511
Koudmani S., Sijacki D., Smith M. C., 2022, MNRAS, 516, 2112
Labbe I. et al., 2024, preprint (arXiv:2412.04557)
Laor A., 2006, ApJ, 643, 112
Latif M. A., Ferrara A., 2016, PASA, 33, e051
Leung G. C. K. et al., 2019, ApJ, 886, 11
Li J., Shen Y., Zhuang M.-Y., 2025, preprint (arXiv:2502.05048)
Lin X. et al., 2026, ApJ, 997, 364
Loeb A., 2024, RNAAS, 8, 182
Ma Y. et al., 2026, ApJ, 1000, 69
Ma Y. et al., 2025b, ApJ, 981, 191
Mac Low M.-M., 1999, ApJ, 524, 169
Mac Low M.-M., Klessen R. S., 2004, Rev. Modern Phys., 76, 125
Maiolino R. et al., 2010, A&A, 517, A47
Maiolino R. et al., 2024, A&A, 691, A145
Maiolino R. et al., 2025a, preprint (arXiv:2505.22567)
Maiolino R. et al., 2025b, MNRAS, 538, 1921
Marconi A., Hunt L. K., 2003, ApJ, 589, L21
Marshall M. A. et al., 2025, A&A, 702, A50
Matthee J. et al., 2024, ApJ, 963, 129
McClymont W. et al., 2025a, MNRAS, 540, 190
McClymont W. et al., 2025b, MNRAS, 544, 513
McClymont W. et al., 2026, MNRAS, 545, staf2092
McConnell N. J., Ma C.-P., 2013, ApJ, 764, 184
Moseley S. H., Arendt R. G., Fixsen D. J., Lindler D., Loose M., Rauscher B. J., 2010, in Holland A. D., Dorn D. A., eds, Proc. SPIE Conf. Ser. Vol. 7742, High Energy, Optical, and Infrared Detectors for Astronomy IV. SPIE, Bellingham, p. 77421B
Nikopoulos G. P., Watson D., Sneppen A., Rusakov V., Heintz K. E., Witstok J., Brammer G., 2025, preprint (arXiv:2510.06362)
Pacucci F., Loeb A., 2025, ApJ, 989, L19
Pacucci F., Narayan R., 2024, ApJ, 976, 96
Perna M. et al., 2023, A&A, 679, A89
Peterson B. M. et al., 2004, ApJ, 613, 682
Planck Collaboration VI, 2020, A&A, 641, A6
Portegies Zwart S. F., Makino J., McMillan S. L. W., Hut P., 1999, A&A, 348, 117
Rauscher B. J. et al., 2012, in Holland A. D., Beletic J. W., eds, Proc. SPIE Conf. Ser. Vol. 8453, High Energy, Optical, and Infrared Detectors for Astronomy V. SPIE, Bellingham, p. 84531F
Rauscher B. J. et al., 2017, PASP, 129, 105003
Rees M. J., 1984, ARA&A, 22, 471
Reines A. E., Volonteri M., 2015, ApJ, 813, 82 (RV15)
Renzini A., 2025, MNRAS, 536, L8
Rieke M. J. et al., 2023, ApJS, 269, 16
Rusakov V. et al., 2026, Nature, 649, 574
Saglia R. P. et al., 2016, ApJ, 818, 47
Shapley A. E., Sanders R. L., Reddy N. A., Topping M. W., Brammer G. B., 2023, ApJ, 954, 157
Silk J., 2017, ApJ, 839, L13
Simmonds C. et al., 2024, MNRAS, 535, 2998
Simmonds C. et al., 2025, MNRAS, 544, 4551
Smith K. C., Howarth I. D., 1998, MNRAS, 299, 1146
Stern J., Laor A., 2012, MNRAS, 423, 600
Stone M. A., Lyu J., Rieke G. H., Alberts S., 2023, ApJ, 953, 180
Storey P. J., Zeippen C. J., 2000, MNRAS, 312, 813
Stott J. P. et al., 2016, MNRAS, 457, 1888
Sun Y. et al., 2025, ApJ, 978, 98
Taylor M. B., 2005, in Shopbell P., Britton M., Ebert R., eds, ASP Conf. Ser. Vol. 347, Astronomical Data Analysis Software and Systems XIV. Astron. Soc. Pac., San Francisco, p. 29
Taylor A. J. et al., 2025, ApJ, 986, 165
Torralba A. et al., 2025, A&A, 707, A75
Trebitsch M., Volonteri M., Dubois Y., Madau P., 2018, MNRAS, 478, 5607
Trinca A. et al., 2024, preprint (arXiv:2412.14248)
Tripodi R. et al., 2025, Nat. Commun., 16, 9830
Übler H. et al., 2023, A&A, 677, A145
van der Wel A. et al., 2022, ApJ, 936, 9
van Rossum G., 1995, CWI Technical Report, CS-R9526
Veilleux S., Cecil G., Bland-Hawthorn J., 2005, ARA&A, 43, 769
Veilleux S., Maiolino R., Bolatto A. D., Aalto S., 2020, A&AR, 28, 2
Wang B. et al., 2024, ApJ, 969, L13

Wang B. et al., 2025, ApJ, 984, 121
Yue M., Eilers A.-C., Ananna T. T., Panagiotou C., Kara E., Miyaji T., 2024, ApJ, 974, L26
Zhou L. et al., 2017, MNRAS, 470, 4573
Zhu H., Tian W., Li A., Zhang M., 2017, MNRAS, 471, 3494

APPENDIX A: ALTERNATIVE MODELS OF BROAD H β AND H α

The double-Gaussian assumption represents a convenient and effective way to capture the observed shape of the H α emission. However, in principle, other line shapes are possible, such as a broken power law or a Lorentzian profile. Here, we test three alternative approaches; a single Gaussian, a Voigt profile (I. Labbe et al. 2024), and a Gaussian with exponential wings (V. Rusakov et al. 2026).

The maximum-likelihood single-Gaussian model is shown in Fig. A1. This model yields a worse fit than the fiducial model, and is actually one of few BLR profiles that is ruled out by the data (in agreement with V. Rusakov et al. 2026), with Δ BIC > 35. The model presents clear excess blueward and redward of the narrow-line H α , which in the fiducial fit is attributed to the narrowest of the two broad Gaussians (cf. Fig 1c). To capture some of this flux, the model uses a broader and redshifted narrow-line, coupled with very strong and very narrow absorption. This is an unfavourable combination, because the redshift of the narrow H α does not agree with the redshift of H β and [O III] λ5007. As a result, the latter two lines, which have lower SNR than narrow H α , are both clipped as outliers. Furthermore, the extremely narrow absorber (having $\sigma_{\rm abs} < 20\,{\rm km\,s^{-1}}$, 3σ upper limit; Fig. A1c) is completely inconsistent with the shape of the Balmer break, which is remarkably smooth (L. J. Furtak et al. 2024; Y. Ma et al. 2025b; J25). More subtle, but still noticeable, is the excess flux around 5.27 and 5.29 μm, also evident as several consecutive pixels with $\chi < -2$ around these wavelengths in Fig. A1(b). In any case, we reject a single broad-line Gaussian with an absorber as a viable model for the BLR in Abell2744-QSO1.

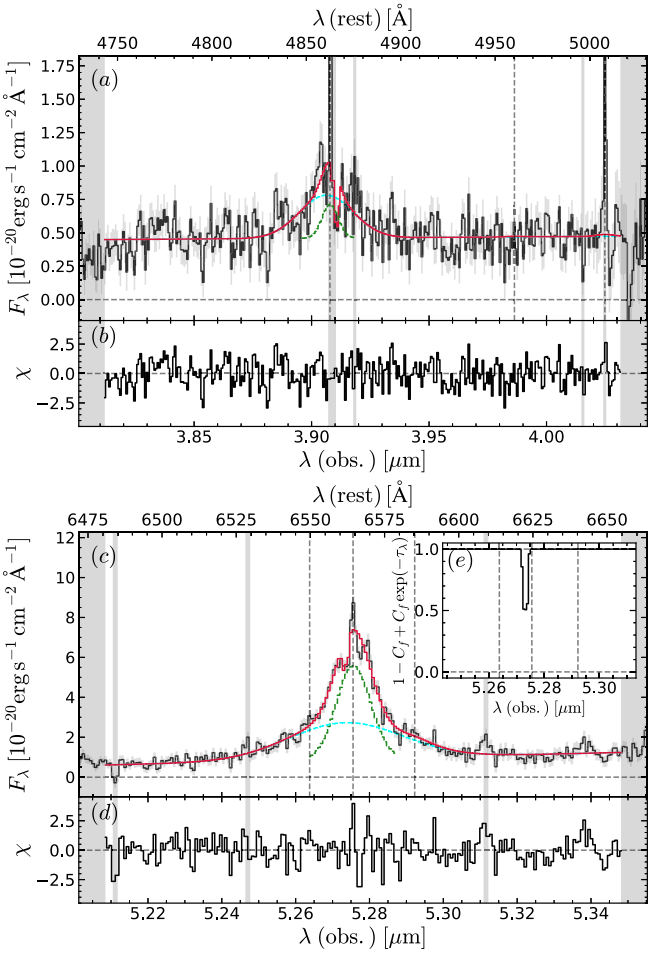

Figure A1. Best-fitting model of H α using a single-Gaussian profile for the broad emission. A single Gaussian does not reproduce the line shape, with the model using the narrow-line component to accommodate the intermediate-width broad Gaussian (green dashed line), and ignoring the narrow lines. This fit yields Δ BIC > 35 relative to the fiducial double-Gaussian model. The panels and line colours are the same as in Fig. 1.

Next we consider a Voigt profile, a more general model than a Lorentzian profile, since the latter reduces to a Voigt profile in the presence of kinematic broadening in the line core. For the case in hand, we have a minimum core broadening of $\sigma = 34\,{\rm km\,s^{-1}}$ due to the spectral resolution of NIRSpec. We obtain $FWHM_{\rm b} = 770^{+50}_{-50}$ km s^{-1} and $\log(M_\bullet/{\rm M}_\odot) = 6.5$; all other quantities are statistically consistent with the fiducial fit. The Voigt model (Fig. A2) provides an adequate characterization of the broad lines, with a marginally worse BIC than the fiducial double-Gaussian model, although the difference is not sufficient for model selection (Δ BIC $= 2$). Around H α only, the model performs even worse (Δ BIC $= 7$). While fit quality alone cannot select Voigt over a double-Gaussian model, we adopt the latter as fiducial model based on other considerations, as explained below for the electron-scattering model.

Finally, we consider a broad-line model given by a single broad Gaussian transmitted through a high column density of ionized gas. This is given by a broad Gaussian (transmitted component), plus a fraction of the same Gaussian convolved with an exponential kernel, motivated by Doppler broadening due to electron scattering (A. Laor 2006; V. Rusakov et al. 2026; see F. D'Eugenio et al. 2025 for our specificformalism). This model yields a satisfactory fit to the data (Fig. A3); specifically, when compared to the fiducial double Gaussian model, we find Δ BIC $= 2$ in favour of the electron-scattering model. The results concerning the absorbing gas are unchanged, because observing noise overcomes systematic uncertainties. This model yields a narrow Gaussian width with, $FWHM_{\rm b} = 670^{+60}_{-60}$ km s^{-1}; applying the calibration of RV15 yields $\log(M_\bullet/{\rm M}_\odot) = 5.9$. Such a low value would reduce the tension with local scaling relations (albeit Abell2744-QSO1 would remain an overmassive outlier in Fig. 4). As noted by V. Rusakov et al. (2026), this model naturally results in a high Eddington ratio, $\lambda_{\rm Edd} = 2.1^{+0.8}_{-0.6}$. However, this $M_\bullet$ measurement is 1.8-dex lower than the direct measurement of I. Juodžbalis et al. (2026a). Such a strong discrepancy argues against the electron-scattering model or – at the very least – its combination with virial scaling relations. More decisive is the finding that the intermediate-width component is spatially extended, unlike the broadest component (I. Juodžbalis et al. 2026a). This argues against a common origin of the two broad components, justifying the adoption of a double Gaussian.

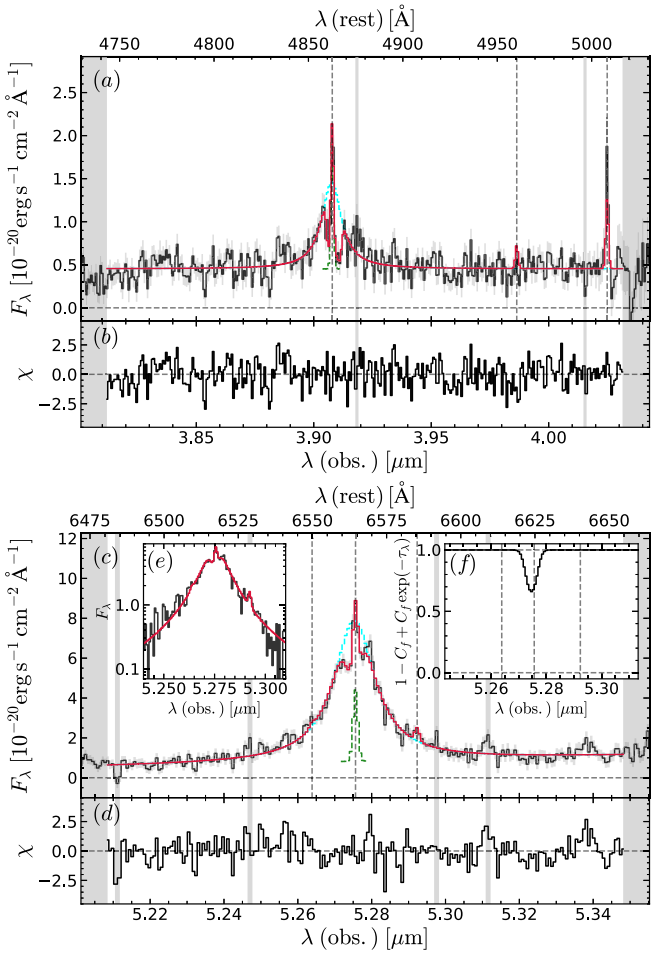

Figure A2. Best-fitting model of H α using a Voigt profile for the broad emission. The Voigt (and Lorentzian) profiles provide an adequate fit to the data (particularly H β), but we disfavour this model based on the fact that the intermediate broad component is spatially resolved (R. Maiolino et al. 2025a; I. Juodžbalis et al. 2026a), while this model uses a single broad component. The panels and line colours are the same as in Fig. 1, except for the broad-line model, which here consists of a single Voigt function (cyan).

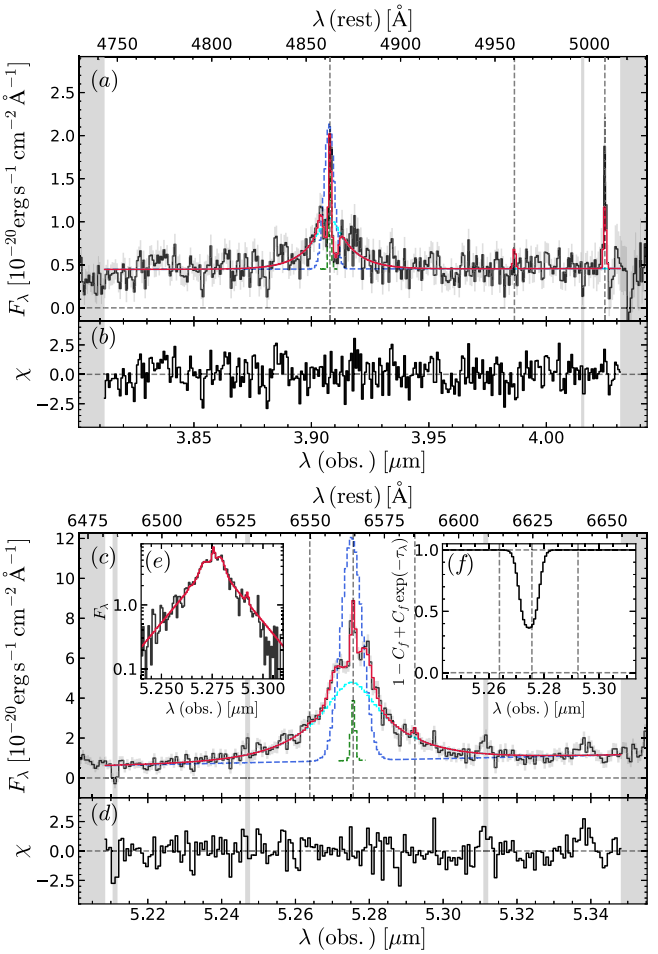

Figure A3. Best-fitting model of H α using the 'exponential' model, where the broad lines are the sum of a single Gaussian (transmitted component) plus a Gaussian convolved with an exponential kernel (scattered component). The exponential model fits the data as well (if not better) than the fiducial double-Gaussian model (Fig. 1), but we exclude this model based on the fact that the intermediate broad component is spatially resolved (R. Maiolino et al. 2025a; I. Juodžbalis et al. 2026a). The panels and line colours are the same as in Fig. 1, except for the blue and cyan model lines, which here represent respectively the transmitted and scattered broad Gaussian.

[1]*Kavli Institute for Cosmology, University of Cambridge, Madingley Road, Cambridge CB3 0HA,UK*
[2]*Cavendish Laboratory – Astrophysics Group, University of Cambridge, 19 JJ Thomson Avenue, Cambridge CB3 0HE, UK*
[3]*Department of Physics and Astronomy, University College London, Gower Street, London WC1E 6BT, UK*
[4]*Centro de Astrobiología (CAB), CSIC–INTA, Cra. de Ajalvir Km. 4, E-28850 Torrejón de Ardoz, Madrid, Spain*
[5]*Max-Planck-Institut für extraterrestrische Physik, Gießenbachstraße 1, D-85748 Garching, Germany*
[6]*Centre for Astrophysics Research, Department of Physics, Astronomy and Mathematics, University of Hertfordshire, Hatfield AL10 9AB, UK*
[7]*Institute of Astronomy, University of Cambridge, Madingley Road, Cambridge CB3 0HA, UK*
[8]*Center for Astrophysics Harvard & Smithsonian, 60 Garden St, Cambridge, MA 02138, USA*
[9]*Department of Physics, University of Oxford, Denys Wilkinson Building, Keble Road, Oxford OX1 3RH, UK*
[10]*Scuola Normale Superiore, Piazza dei Cavalieri 7, I-56126 Pisa, Italy*
[11]*Sorbonne Université, CNRS, UMR 7095, Institut d'Astrophysique de Paris, 98 bis bd Arago, F-75014 Paris, France*
[12]*INAF – Osservatorio Astrofisico di Arcetri, Largo E. Fermi 5, I-50127 Firenze, Italy*
[13]*Dipartimento di Fisica e Astronomia 'G. Galilei', Università di Padova, Vicolo dell'Osservatorio 3, I-35122 Padova, Italy*
[14]*INAF – Osservatorio Astronomico di Padova, Vicolo dell'Osservatorio 5, I-35122 Padova, Italy*
[15]*Jeremiah Horrocks Institute, University of Central Lancashire, Preston PR1 2HE, UK*
[16]*Kavli Institute for Astronomy and Astrophysics, Peking University, Beijing 100871, China*
[17]*Steward Observatory, University of Arizona, 933 N. Cherry Ave., Tucson, AZ 85721, USA*
[18]*Dipartimento di Fisica e Astronomia, Università di Firenze, via G. Sansone 1, I-50019 Sesto F.no (Firenze), Italy*
[19]*Dipartimento di Fisica e Astronomia, Università di Bologna, via Gobetti 93/2, I-40129 Bologna, Italy*
[20]*INAF – Osservatorio di Astrofisica e Scienza dello Spazio di Bologna, via Gobetti 93/3, I-40129 Bologna, Italy*
[21]*Department for Astrophysical and Planetary Science, University of Colorado, Boulder, CO 80309, USA*
[22]*Department of Astronomy and Astrophysics, University of California, Santa Cruz, Santa Cruz, CA 95064, USA*
[23]*Dipartimento di Fisica, Sapienza Università di Roma, Piazzale Aldo Moro 2, I-00185 Roma, Italy*
[24]*NRC Herzberg, 5071 West Saanich Rd, Victoria, BC V9E 2E7, Canada*
[25]*Cosmic Dawn Center (DAWN), Copenhagen, Denmark*
[26]*Niels Bohr Institute, University of Copenhagen, Jagtvej 128, DK-2200 Copenhagen, Denmark*
[27]*Department of Astronomy, University of Geneva, Chemin Pegasi 51, CH-1290 Versoix, Switzerland*

This paper has been typeset from a TEX/LATEX file prepared by the author.